

See discussions, stats, and author profiles for this publication at: <https://www.researchgate.net/publication/231666321>

# Nucleation, Growth, and Relaxation of Thin Films: Metal(100) Homoepitaxial Systems

ARTICLE · JANUARY 2000

DOI: 10.1021/jp9933471

---

CITATIONS

34

---

READS

8

2 AUTHORS:



[Patricia A Thiel](#)

Iowa State University

**350** PUBLICATIONS **9,476** CITATIONS

[SEE PROFILE](#)



[James Evans](#)

Iowa State University

**260** PUBLICATIONS **6,449** CITATIONS

[SEE PROFILE](#)

## FEATURE ARTICLE

### Nucleation, Growth, and Relaxation of Thin Films: Metal(100) Homoepitaxial Systems

P. A. Thiel<sup>\*,†</sup> and J. W. Evans<sup>‡</sup>

*Departments of Chemistry and Mathematics, and Ames Laboratory, Iowa State University, Ames, Iowa 50011*

*Received: September 20, 1999; In Final Form: November 19, 1999*

We describe work in our laboratory that has shed new light on nucleation, growth, and relaxation processes in thin metal films. The progress comes from the synergistic and synchronous implementation of theory and experiment, which reveals surprising secrets hidden a very simple model system.

#### 1. Introduction

Nucleation and growth of materials are kinetically-determined processes. As such, they typically lead to nonequilibrium morphologies, which relax in some fashion afterward. This set of topics—nucleation, growth, and subsequent relaxation (NGR)—provides a framework for understanding many aspects of the world around us, from geological erosion to pharmaceutical sedimentation to nano-fabrication. As such, the topic is immensely important and scientifically ancient. This paper deals with one small, but important, arena in which fresh insights about NGR are emerging, namely, epitaxial metal films on metal surfaces. The discussion focuses largely on work from our own group, although beautiful work is also being carried out in a number of other laboratories around the world. In our case, new insights are due mainly to the *synergistic and synchronous* employment of experiment and theory. In the experiments, we utilize two techniques—scanning tunneling microscopy and high-resolution, low-energy electron diffraction—which are still relatively new on the experimental landscape, and which are complementary. In the theory, we develop suitable lattice-gas models which are analyzed with kinetic Monte Carlo (KMC) simulations, an approach which yields more precise, even fundamentally different, results than more traditional mean-field rate-equation analyses. The experiments and theory can only

be coupled so powerfully because of the simplicity of the physical system. That system is self-growth (homoepitaxy) on a single-crystal surface (fcc(100)), provoked by vapor deposition in ultrahigh vacuum. The material is Ag, which is one of the most inert metals and, hence, relatively insensitive to contamination, which can be a troublesome experimental variable even in ultrahigh vacuum.<sup>1</sup> In spite of the simplicity of the system, the understanding we gain can be applied to a variety of more complex topics, e.g. microelectronics, as has already been shown in part.<sup>2</sup>

A system that is driven out of equilibrium (by deposition, in our case) will naturally return to its equilibrium state, the latter being uniquely defined by the Hamiltonian. This is a well-known principle, but perhaps what is not appreciated is that there are many kinetic pathways available for equilibration or relaxation. Some are obvious, some are not, and those chosen are strongly system dependent. In our work, we have found surprises in the equilibration pathways, as well as in the growth processes themselves.

The advantage of studying homoepitaxy on a single-crystal surface is that the thermodynamically dictated structures are well-known. In equilibrium, the film must grow smoothly, i.e., in perfect layer-by-layer sequence. (This is strictly true only below the roughening transition temperature, a condition that is met throughout our discussion.) Within an individual partially filled layer, the atoms are driven to aggregate in a single large island. (This is strictly true only below the critical temperature for 2D-phase separation, a condition that again is met throughout

\* Corresponding author.

<sup>†</sup> Department of Chemistry.

<sup>‡</sup> Department of Mathematics.

our discussion.) Furthermore, the equilibrium shape, or imprint, of the island(s) in a partially filled layer is dictated by the symmetry of the underlying substrate, plus the nature of adatom interactions in the island. In reality, the vertical profile of the film is not smooth, the lateral profile is not characterized by a single large island, and the shape of the island(s) can be highly irregular. The deviations from equilibrium occur because growth is (typically) dominated by kinetics, not thermodynamics. Hence, in a homoepitaxial film one can identify nonequilibrium configurations readily and monitor their decay to a predictable end point. This is not necessarily true for systems that are even slightly more complex, such as heteroepitaxial films.

This paper deals with five main phenomena, in five main sections. The first (section 3) is nucleation and growth of islands within a single layer. Because the film does not grow in perfect layer-by-layer fashion, this topic can be studied most cleanly within the first layer, i.e., in the *submonolayer* regime of growth. The second (section 4) deals with relaxation of the array of submonolayer islands toward a single large island. This process is called *coarsening*. The third (section 5) deals with the *reshaping* of far-from-equilibrium two-dimensional nanostructures toward forms consistent with the two-dimensional packing arrangement imposed by the substrate geometry (and the adatom interactions). The fourth (section 6) deals with the roughness of multilayer films that results from the deposition process, an effect known as *kinetic roughening*. The fifth (section 7) deals with relaxation, or *smoothing*, of the multilayer films. These five sections are supplemented by a description of key experimental and theoretical details, which follows immediately.

## 2. Experimental and Theoretical Details

Our experiments were performed at  $6 \times 10^{-11}$  to  $2 \times 10^{-10}$  Torr in an ultrahigh vacuum chamber equipped with both an Omicron high-resolution, low-energy electron diffraction (HR-LEED) system, and an Omicron room-temperature scanning-tunneling microscope (STM). Silver was deposited on a Ag(100) crystal (surface lattice constant  $a = 2.89$  Å) from a resistively heated liquid-nitrogen-shrouded source. The STM images of island distributions used in our analyses<sup>3–6</sup> were obtained on  $>2000$  Å wide terraces. Images were obtained under conditions of low resolution so as to minimize the STM tip–surface interaction. The first STM image was obtained typically 15–40 min after deposition, and subsequent postdeposition images every 5–15 min.

In the HRLEED analysis,<sup>7</sup> an Ag crystal with typical terrace widths of  $L_{\text{terr}} \approx 1000$  Å was used for studies at 295 K, and a poorer quality crystal with  $L_{\text{terr}} \approx 600$  Å was used for 280–170 K. In all cases, terrace widths are far larger than island separations. HRLEED intensities were obtained near an out-of-phase condition for destructive interference between scattering from successive layers in Ag/Ag(100). At the (0,0) beam corresponding to zero lateral momentum transfer, the out-of-phase condition corresponds to  $q_z b = (2n + 1)\pi$ , for integer  $n$ . Here,  $q_z$  is the vertical momentum transfer, and  $b = 2.05$  Å is the interlayer spacing for the fcc Ag crystal. We choose an energy of 110.4 eV, corresponding to  $n = 3$ . All profiles shown were taken in the [110] direction, and measured within about 2.5–5 min after deposition. The flux was calibrated from the Bragg intensity oscillations.

The general strategy adopted in our theoretical lattice-gas treatment of film growth is to develop “tailored models” which are as simple as possible, yet capture the essential features of the process for the system of interest (e.g., the formation of near-square islands within each layer). Furthermore, we adopt

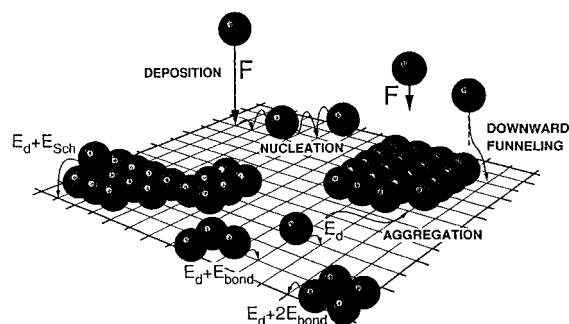


**Figure 1.** Atomistic processes invoked in the model of metal film growth.

the approach of first analyzing the simplest experimental regime (i.e., irreversible submonolayer island formation at lower temperatures), where there is essentially one relevant unknown “free parameter” (the terrace diffusion rate), which can be determined by matching theory and experiment. We then extend the model to handle other regimes (e.g., reversible island formation, or multilayer growth), adding additional processes and associated free parameters or rates, which are again determined one at a time by matching experiment. These models can be analyzed efficiently on the time and length scales relevant for experiment utilizing kinetic Monte Carlo (KMC) simulation. It is particularly instructive to also develop analytic descriptions of growth behavior, utilizing either appropriate rate or diffusion equations. Indeed, the latter was the traditional approach to modeling film growth, dating back to the 1960s. Thus, we shall also comment on this approach, plus recent refinements. A similar strategy is utilized in analyzing equilibration or relaxation processes, i.e., development of tailored models capturing the essential features of the process, which are then analyzed with KMC simulation or utilizing analytic formulations.

## 3. Nucleation and Growth of Islands in the Submonolayer Regime

**3.1. The Basic Picture.** As noted above, the deviations from equilibrium structures are mainly due to the kinetic processes that dominate growth. (There is also some contribution from the nonideality of the real surface, mainly the presence of steps.) The kinetic processes invoked in this paper are illustrated in Figure 1. These include deposition of single atoms on flat terraces, downward deflection of single atoms deposited at step edges (downward funneling); single-atom diffusion (which may or may not involve place-exchange with the underlying substrate); nucleation of islands by diffusing atoms; incorporation of a diffusing atom into an existing island edge; and diffusion of an atom over a step edge. It is also conceivable that various diffusion processes involving clusters, rather than just single adatoms, are important during growth. However, as we show below, it appears that diffusion of dimers or larger clusters does not contribute significantly *during* growth on Ag(100), although diffusion is clearly evident *after* deposition stops. This seeming contradiction simply reflects the vastly different time scales that are relevant during deposition vs for later observation. Whether or not bond-breaking or bond-scission processes are operative will depend on the surface temperature. As might be expected, bond-forming processes (nucleation, incorporation at island edges) are irreversible at low temperatures, and reversible at high temperatures.

Whether any of the processes in Figure 1 contributes to film growth depends, of course, on their rate relative to the rate of deposition, defined as  $F$ . In most laboratories, deposition rates

of about 0.01 layer/s ( $10^{13}$  atoms/(s·cm<sup>2</sup>), or 0.01 atom/(s·site)) are practical and convenient, implying that a process with a rate below about 0.01 event/s has little chance of affecting growth. At room temperature, this corresponds to an upper limit on the activation barrier for contributing processes of about 0.9 eV (assuming an attempt frequency of  $10^{13}$ /s). In fact, some processes must be active on a much shorter time scale than that of deposition to significantly influence growth (e.g., bond-breaking must be operative on the time scale of aggregation of atoms with islands, or else bonds do not have a chance to break before the atoms are enclosed in the interior of islands).

Vacancy diffusion is not included in Figure 1. This process may be important during relaxation,<sup>8</sup> cluster diffusion,<sup>9</sup> or etching.<sup>10</sup> However, it is almost certainly irrelevant under growth conditions, because deposition serves to supersaturate the surface with free adatoms. Other processes may also be important which have not yet been fathomed. However, the processes pictured in Figure 1 seem to serve as an adequate description of Ag-(100) homoepitaxy, since most of the experimental results are well described, and even predicted, by the Monte Carlo simulations.

Transient mobility, i.e., long-range ballistic motion of an atom impinging on the surface, which might derive from the energy released in forming the atom–substrate bond, is not included in Figure 1. Although this interesting process was originally proposed by Egelhoff and co-workers as an important factor in metal homoepitaxy,<sup>11</sup> it has not been supported by theoretical<sup>12,13</sup> or experimental<sup>14,15</sup> work. Presumably, the process is inoperative because there is a perfect mass match for energy transfer in homoepitaxy, and because phonons dissipate energy very efficiently in metals. (Transient mobility does occur in situations where energy dissipation is not efficient, e.g. in semiconductor growth<sup>16</sup> or in adsorption of small molecules on metals.<sup>17</sup>)

The processes in Figure 1 have an interesting consequence for the distribution of island *positions*. Are the islands distributed randomly? The answer is “no”. The reason is that adatom density surrounding islands is depleted since island edges act as sinks (actually, perfect sinks at low  $T$ , where adatom capture is irreversible). This leads to a depletion in the rate of nucleation near existing islands, and thus a so-called depletion zone around islands.<sup>18–20</sup> We note that nucleation-mediated growth does not necessarily occur. If temperature is high and single-atom diffusion is fast, atoms reach existing steps (step flow). If temperature is low and single-atom diffusion is inoperative, “quasi-random deposition” controlled by downward funneling can predominate. Nucleation and growth only occur for specific ranges of temperature, diffusion rate, and step density.<sup>21,22</sup>

The processes in Figure 1 have been used as the ingredients for basically two different theoretical formulations. The first, and more established, is a rate-equation analysis.<sup>18,19</sup> The second is the development of lattice-gas models, which are investigated using KMC simulation. The second approach involves fewer assumptions; in particular, the mean-field assumption is not made. It has been an ongoing theme of our work to compare the rate-equation results with Monte Carlo simulations, thereby testing the assumptions inherent in the former, and comparing both with experimental data where possible. The main characteristics of the film that we focus on, in this submonolayer regime, will be average island density and island size distribution.

**3.2. The Nucleation Process.** The mean island density can be observed directly with STM, and indirectly with HRLEED. First, let us review briefly the prediction for island density from the rate-equation approach. Below,  $\theta$  denotes the coverage (in

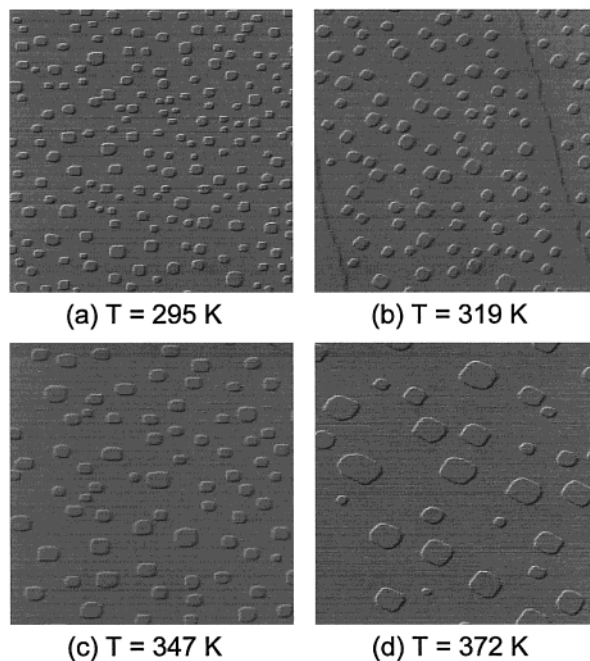


**Figure 2.** STM images ( $176 \times 176$  nm<sup>2</sup>) of Ag island distributions on Ag(100) after deposition of about 0.1 monolayer with  $F \approx 0.06$  monolayer/s at (a) 295 K; (b) 320 K; (c) 350 K; (d) 375 K. Reprinted from refs 5 and 6, with permission. Copyright 1997, 1998 Elsevier Science. Note that the orientation of the surface is different in 2b,d than in 2a,c.

monolayers), and  $h = \nu \exp[-E_d/(k_B T)]$  denotes the rate for adatom hopping across the terrace to each adjacent site (with activation barrier  $E_d$ , and attempt frequency  $\nu$ ). Since  $F$  denotes the deposition rate (in monolayers per unit time), one has  $\theta = Ft$ . The density (per adsorption site on the fcc(100) surface) of diffusing adatoms is denoted by  $N_1$ , and of islands of  $s$  atoms is denoted by  $N_s$ . The mean island density,  $N_{av} = \sum_{s>1} N_s$ , determines the average island separation,  $L_{av} = (N_{av})^{-1/2}$  (in units of the lattice constant,  $a$ ), and average island size,  $s_{av} \approx \theta/N_{av}$  (measured in atoms).

The rate-equation analysis is particularly simple for island formation in the regime of low coverage, because there growth-induced coalescence (merging of islands as they grow into one another) can be neglected. (Growth-induced coalescence typically begins around 0.25–0.35 monolayer.) The rate of aggregation, between diffusing atoms and islands of size  $s$ , is given by  $R_{agg}(s) = h\sigma_s N_1 N_s$ , where  $\sigma_s$  denotes the “capture number” for islands of size  $s$ . The rate of “direct capture,” by deposition on top of or directly adjacent to an island of size  $s$ , equals  $F\kappa_s N_s$ , where  $\kappa_s \approx s + 4\sqrt{s}$  for near-square islands. (Because adsorption sites on Ag(100) form a square lattice, the islands tend to adopt a square shape, as shown in Figure 2a.) For irreversible island formation, one then has<sup>18–20</sup>

$$dN_1/dt \approx F(1 - \theta) - 2R_{agg}(1) - \sum_{s>1} R_{agg}(s)$$

$$dN_s/dt \approx F(\kappa_{s-1}N_{s-1} - \kappa_s N_s) + R_{agg}(s-1) - R_{agg}(s) \quad (1)$$

To determine the mean island density,  $N_{av}$ , the eqs 1 are often reduced to

$$dN_1/dt \approx F(1 - \theta) - h\sigma_{av}N_1N_{av}$$

$$dN_{av}/dt \approx h\sigma_1(N_1)^2 \quad (2)$$

where  $\sigma_{av} = \sum_{s>1} \sigma_s N_s / \sum_{s>1} N_s$ . Then, using the steady-state



**TABLE 1: Values of the Island Density,  $N_{av}$  (per site), from Experiment and Simulations with  $F = 0.06$  monolayer/s**

	295 K	319 K	347 K	372 K
experimental $N_{av}$	$8.5 \times 10^{-4}$	$6.4 \times 10^{-4}$	$3.2 \times 10^{-4}$	$0.89 \times 10^{-4}$
$E_{bond} = 0.3$ eV,	$8.5 \times 10^{-4}$	$5.4 \times 10^{-4}$	$2.7 \times 10^{-4}$	$1.01 \times 10^{-4}$
$E_d = 0.38$ eV				
$E_{bond} = \infty$ ,	$8.5 \times 10^{-4}$	$5.8 \times 10^{-4}$	$4.0 \times 10^{-4}$	$3.0 \times 10^{-4}$
$E_d = 0.38$ eV ( $i = 1$ )				

condition,  $dN_i/dt \approx 0$ , one immediately obtains from integration of (2) that  $N_{av} \sim C(\theta)(h/F)^{-1/3}$  for large  $h/F$ , assuming that  $\sigma_{av}$  depends only on  $\theta$ . We emphasize that this key result is valid only in the case where island formation is irreversible. Our simulations for irreversible formation of square islands<sup>23,24</sup> reveal that it is almost exactly satisfied:  $N_{av} \sim (h/F)^{-\chi}$ , with  $\chi \approx 0.31$  for  $h/F \approx 10^7$ – $10^9$ , and with a fairly weak dependence on  $\theta$  around 0.1 monolayer.

Our early STM studies,<sup>5,6</sup> focusing on submonolayer island formation at 295 K (Figure 2a), showed that  $N_{av} \approx 1.9 \times 10^{-3} F\%$ /site, for  $F$  between 0.002 and 0.1 monolayer/s and  $\theta$  between 0.03 and 0.2 monolayer. The value of the scaling exponent,  $\chi$ , was 0.31, demonstrating that nucleation of two atoms is indeed irreversible at 295 K. The experimental data were incompatible with significant dimer mobility, for which an exponent of 0.4 was predicted from theory. However, our earlier data may have been slightly affected by adlayer coarsening before STM imaging (mainly for  $\theta \leq 0.05$  monolayer), and growth-induced coalescence (for  $\theta \geq 0.25$  monolayer). Both effects can lead to underestimation of  $N_{av}$ . Extensive new data (involving a total of about 650 islands) under conditions chosen to minimize these effects suggests a slightly higher  $N_{av} \approx 2.4 \times 10^{-3} F\%$ /site, using  $\chi \approx 0.31$ . Extraction of an estimate of the terrace diffusion barrier,  $E_d$ , from this behavior is discussed below in section 3.3.

Of course, at high enough temperature, the collision or bonding of two diffusing atoms must become a reversible process. To examine the transition to this regime, we monitored the decrease in  $N_{av}$  with increasing  $T$ , from 295 to 370 K, at fixed flux and coverage (see Table 1). Associated STM images are shown in Figure 2. The Arrhenius slope of  $N_{av}$  versus  $T$  increases continuously with increasing  $T$  above about 320 K, indicating the onset of reversible bond formation. To model this behavior, we incorporated bond scission into the KMC simulations, assuming that bond breaking is controlled by finite nearest-neighbor (NN) pairwise interactions of strength  $E_{bond}$ .<sup>5,6</sup> The decrease of  $N_{av}$  above 320 K is best fit in this model by  $E_{bond} \approx 0.3$  eV, with  $\nu \approx 10^{13}$ /s. See Table 1. (The fit also assumes an  $E_d$  which is consistent with the value derived in section 3.3.)

It should be emphasized that this value should be interpreted as an *effective* NN interaction strength, since the actual adspecies interactions undoubtedly have a more complex form than NN pairwise including many-body components. Indeed, the values for NN interactions derived from the above approach have been critiqued by Feibelman<sup>25</sup> as potentially being far too large for various metal homoepitaxial systems. This view is based on the known value for the W/W(110) system, and the idea that adspecies interactions should scale with the bulk cohesive energy for the metal crystal. While to date there have been no published ab initio calculations for the Ag ad-dimer bond strength on Ag(100), there has been a sophisticated GGA analysis of the bonding of an Ag adatom to a close-packed [110] step edge.<sup>26,27</sup> The value is slightly higher than 0.3 eV, entirely consistent with our value and the expectation that dimer bonding should be slightly weaker than bonding to the step edge (a feature supported by semiempirical studies of energetics).

For the rate-equation description of this transition, additional

**TABLE 2: Values for  $L_c = 4\pi/d^*$  versus  $T$  for 0.3 monolayer Ag/Ag(100) with  $F = 2$ – $4 \times 10^{-3}$  monolayer/s**

	180 K	195 K	230 K	240 K	255 K	280 K	295 K
$L_c$ (Å)	62	72	123	156	217	287	299

terms must be included in eq 1 reflecting the possibility of island dissociation via bond scission. When this is done, the MF equations predict that the transition occurs much lower in temperature, for the same energetic parameters as derived from the KMC simulation.<sup>5,6,20,28</sup> This failure is associated with the frequent recombination of a dissociating dimer due to the recurrence of 2D random walks.<sup>29</sup> In a mathematical sense, this recurrence can be viewed in terms of Polya's theorem, which *requires* that a random walker on an infinite 2D lattice must eventually return to its point of origin. This recurrence enhances the recombination probability and effectively stabilizes the dimer.

To summarize this subsection, we have used measurements of average island density vs flux, and vs temperature, to extract fundamental information about the nucleation event on Ag(100). In so doing, we have also compared rate-equation analysis with KMC in extracting information from the average island size. The two approaches yield very comparable results in the regime of irreversible nucleation, but not at higher temperatures where nucleation becomes irreversible.

**3.3. Single-Atom Diffusion Barrier.** With experimental information on  $N_{av}$ , in hand, we can go on to extract the barrier to single-atom diffusion by direct comparison with simulation. Our early data implied that  $h \approx 3 \times 10^6$ /s at 295 K, so  $E_d \approx 0.38$  eV using  $\nu \approx 10^{13}$ /s.<sup>5,6</sup> Our later data leads to a revised estimate of  $E_d \approx 0.40$  eV, again using  $\nu \approx 10^{13}$ /s.

It is more desirable (and conventional) to determine  $E_d$  from the temperature dependence of  $N_{av}$ , since then no attempt frequency need be assumed. This can best be done in the regime below about 320 K where island formation is irreversible.<sup>18–20</sup> It is also desirable to complement STM data with information which reflects a larger spatial area, hence obtaining better statistics. To achieve both these ends, we have exploited HRLEED. HRLEED intensities reflect  $N_{av}$  because the depletion of nearby pairs of islands leads to a well-defined real-space characteristic length,  $L_c \propto L_{av} = (N_{av})^{-1/2}$ . This produces a ring in the diffraction profile (as shown in Figure 11 later in section 6.3) with diameter  $d^* = 4\pi/L_c$ .<sup>23,24</sup> Invariably,  $L_c$  is identified with  $L_{av}$ , although it is nontrivial to determine the precise proportionality constant which relates these quantities. From KMC-simulated films for Ag(100), we find that  $L_{av} \approx L_c/\lambda(\theta)$ , where  $\lambda(\theta)$  increases with  $\theta$ , and  $\lambda(0.3) \approx 1.7$ .<sup>7</sup> However, proportionality between  $L_{av}$  and  $L_c$  (for fixed  $\theta$ ) is sufficient to determine  $E_d$ . As shown in Table 2,  $L_c$  increases as  $T$  increases, reflecting again a decrease in  $N_{av}$ . We obtain  $E_d \approx 0.40 \pm 0.04$  eV from the Arrhenius slope ( $E_d/6$ ) of  $L_c$  [cf. (3)], consistent with the results of the above STM analysis.

This value, the single-atom diffusion barrier on Ag, is a fundamental quantity which is not readily measured by other experimental techniques. The technique of choice for single-atom diffusion barriers is field ion microscopy, which cannot be used for soft metals such as Ag. Another approach is to use some technique, such as LEED, to measure the diffusion onset at low temperatures as reflected by some change in film morphology.<sup>30</sup> Such an estimate of 0.4 eV is available from a low-energy ion scattering study.<sup>31</sup> However, this approach yields rougher estimates because of uncertainty in statistics and in the diffusion-onset mechanism, and because the preexponential must again be assumed. A GGA ab initio electronic structure calculation yielded a value of  $0.45 \pm 0.05$  eV.<sup>26,27</sup>

To summarize this subsection, we have used measurements of average island density vs flux and vs temperature, in the regime of irreversible nucleation, to extract the single-atom diffusion barrier on Ag(100). In this case, there is no difference between the results from rate-equation analysis and KMC. However, a much different situation is described in the following section.

**3.4. Information about the Island Size Distribution.** The island size distribution,  $N_s$ , has been analyzed and discussed extensively for decades, but a fundamental breakthrough in our understanding came only recently.<sup>32–34</sup> The form of (1) suggests that the shape of this distribution should be controlled by the size dependence of the capture number,  $\sigma_s$ . (This is strictly true only at low  $\theta$ , where capture due to impingement directly at an island edge, or on top of an existing island, can be neglected.) Indeed, one of us (J.W.E.), together with Maria Bartelt at Sandia National Laboratories Livermore, recently showed that if these capture numbers have the scaling form  $\sigma_s/\sigma_{av} \approx C(s/s_{av})$ , independent of  $\theta$ , then for large  $s_{av}$ , the size distribution has the form<sup>35,36</sup>

$$N_s \approx \theta(s_{av})^{-2} f(s/s_{av}) \quad (3)$$

where

$$f(x) = f(0) \exp\left\{\int_0^x dy [(2\varpi - 1) - dC(y)/dy]/[C(y) - \varpi y]\right\}$$

and  $s_{av} \sim \theta^\varpi$ , with  $\varpi$  assumed constant. Equation 3 gives the explicit form of the relationship between the scaling function for the island size distribution,  $f$ , and that for the capture numbers,  $C$ . Previous analytic postulates or determinations for its form have actually been qualitatively incorrect in one way or another. Traditional mean-field descriptions had yielded capture numbers,  $\sigma_s$ , slowly increasing with size,<sup>18,19,37</sup> which from (3) produces a very sharp shape to the island size distribution. The actual increase is faster (see below), producing a smoother shape.<sup>35,36</sup>

Hence, the dependence of diffusion-mediated adatom capture on island size controls the form of the island size distribution. However, actually determining the capture number experimentally is difficult. For Ag(100), we have done this by combining STM experiments with KMC simulations as follows. Experimental island distributions of the type shown in Figure 2, but with  $\theta \approx 0.1$  monolayer, are used as the starting point. The sizes and positions of the islands are input to KMC simulations of subsequent growth.<sup>34</sup> From such simulations, we can quantify the rate at which various islands capture atoms, and thus obtain  $\sigma_s/\sigma_{av}$  versus  $s/s_{av}$ .

A previous study, in a different epitaxial system, had proven the validity of such a hybrid STM-KMC approach in determining  $\sigma_s/\sigma_{av}$  versus  $s/s_{av}$  by comparing the hybrid approach with a purely experimental measurement. In the pure experiment, it had been possible to distinguish between the results of two successive depositions because the metal atoms were chemically different, thus allowing measurement of the incremental growth of each island.<sup>32,33</sup>

The result for Ag(100) homoepitaxy is shown in Figure 3a. The quasi-linear increase of  $\sigma_s$  with  $s$  at large sizes is qualitatively distinct from the much slower increase predicted by mean-field theories (MFT). It derives from the feature ignored in MFT that larger islands have larger surrounding areas free of other islands.<sup>32–36</sup> The origin of this behavior has been traced to the crucial island nucleation process which is concentrated at the very beginning of deposition. The first

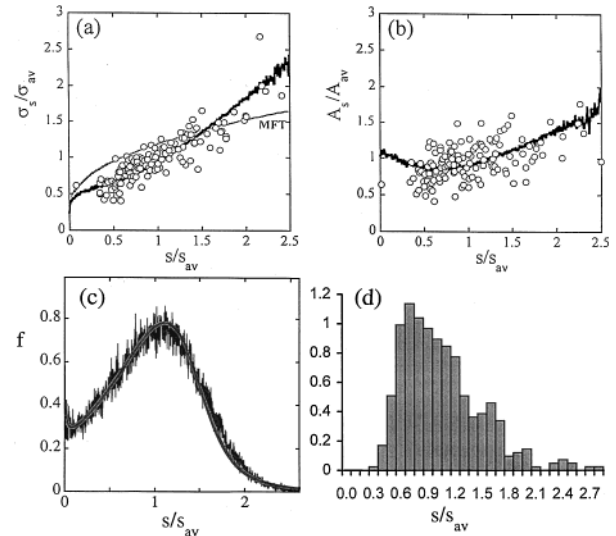


**Figure 3.** (a)  $\sigma_s/\sigma_{av}$  versus  $s/s_{av}$ . (b)  $A_s/A_{av}$  versus  $s/s_{av}$ , for experimental island arrays at 295 K, similar to Figure 2a (symbols). Solid lines show consistent results obtained from simulations of our canonical model for irreversible formation of square islands.<sup>23,24</sup> The distinct mean-field behavior is also shown. Reprinted with permission from ref 59. Copyright 1998 Elsevier Science. (c) The scaled island size distribution from simulations of the canonical model,<sup>23,24</sup> and from eq 3 using the form of  $C(x)$  from (a), and choosing  $\varpi = 0.87$ . Reprinted with permission from ref 34. Copyright 1999 American Physical Society. (d) Experimental scaled island size distribution for Ag/Ag(100) at 295 K. Reprinted with permission from ref 43. Copyright 1999 American Institute of Physics.

islands formed have larger surrounding cells or capture zones (see below) than those formed subsequently. This builds in an initial strong size dependence to capture, and correlations between island size and separation, which persist during island growth. Some initial attempts have been made to quantitatively characterize this behavior based on a theory for the evolution of capture zones.<sup>20</sup>

This geometric interpretation of deviations from MFT is most directly confirmed by performing a standard Voronoi tessellation of the surface based on the island centers.<sup>32–34</sup> A Voronoi tessellation is simply a means of partitioning the surface into cells, such that points within a Voronoi cell (VC) associated with a given island are closer to the center of that island than to the centers of other islands. See Figure 4a. If  $A_s$  is the area of the VC *not* covered by an island of size  $s$ , then Figure 3b shows that  $A_s/A_{av}$  increases with  $s/s_{av}$  in a way similar to that of  $\sigma_s/\sigma_{av}$ . However, these VC areas do not exactly describe the rate of capture by various islands. A much more precise description of capture rates is provided using the areas of the “edge cells” (EC’s) in a Voronoi-type tessellation based on the distance from island edges (rather than centers).<sup>34</sup> See Figure 4b.

Of course, being purely geometric constructions, neither the VC’s or the EC’s precisely describe adatom capture. However, we have shown that an exact description is possible if one incorporates the physics of diffusion-mediated capture by analyzing the equation

$$\partial/\partial t N_1 \approx F + D_{terr} \nabla^2 N_1 \approx 0 \quad (4)$$

for the quasi-steady-state density of deposited adatoms which diffuse to and are irreversibly captured at island edges (where one imposes the boundary condition  $N_1 = 0$ ).<sup>32–34</sup> Here,  $D_{terr} = a^2 h$  is the terrace diffusion coefficient, where  $a = 2.89$  Å is the surface lattice constant. From the solution of this steady-

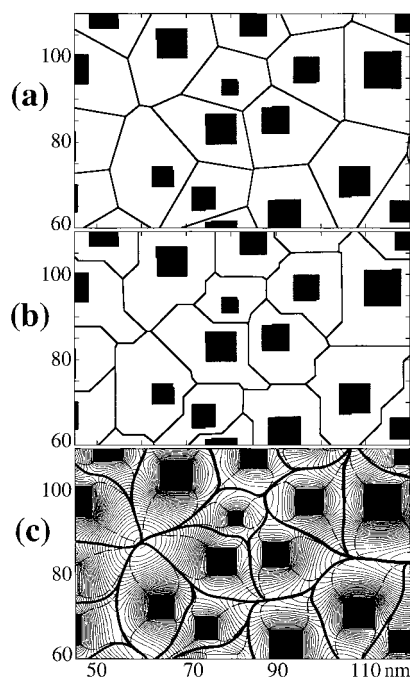


**Figure 4.** (a) VC's; (b) EC's; and (c) DC's (thick solid lines) together with contours for the steady-state  $N_1$  (thin solid lines), for a portion of an experimental island distribution at 295 K. Reprinted with permission from ref 34. Copyright 1999 American Physical Society.

state diffusion equation, each point on the surface is uniquely assigned to a specific island by following the diffusive flux lines from that point to an island. In this way, one can construct a tessellation of the surface into “diffusion cells” (DC's), the areas of which are in *exact proportion* to the capture rates for islands (a result which follows from Gauss' theorem). Such a tessellation is shown in Figure 4c for a small portion of the experimental island distribution, and can be compared with the corresponding VC and EC tessellations in Figure 4a,b.

Inserting the above form for the size dependence of the capture numbers into (3) reproduces the shape of the island size distribution obtained from simulations of irreversible formation of near-square islands.<sup>23,24</sup> See Figure 3c. Here, we use a value of  $\varpi \approx 0.87$  (i.e.,  $s_{av} \sim \theta^{0.87}$ ) reflecting an enhanced tendency for saturation of the density of islands of finite extent,<sup>34</sup>  $N_{av} \sim \theta/s_{av} \sim \theta^{0.13}$ , relative to “point islands” where<sup>38</sup>  $\varpi \approx 2/3$  (i.e.,  $s_{av} \sim \theta^{0.66}$ ) and  $N_{av} \sim \theta^{1/3}$ . The experimental island size distribution, shown in Figure 3d, is roughly consistent with theory allowing that some smaller islands are necessarily lost due to coarsening before STM imaging (see section 4.3), or are not resolved.

In summary, mean-field theories fail to describe the size dependence of the capture number, and hence, the island size distributions. Our KMC simulations show why this is so: the capture number is controlled by the environment of each individual island (the empty space surrounding it) which depends on its size, contrasting the mean-field assumption.

#### 4. Coarsening in the Submonolayer Regime at 295 K

**4.1. Background.** Coarsening is a phenomenon which impacts diverse areas, from sintering of supported catalysts, to lifetimes of nanoscale structures. On a more fundamental level, the equilibration or coarsening of systems undergoing phase-separation has been studied for decades experimentally, and also theoretically using generic lattice-gas models of statistical mechanics.<sup>39</sup> However, it should be recognized that such generic modeling cannot predict the competition between kinetic

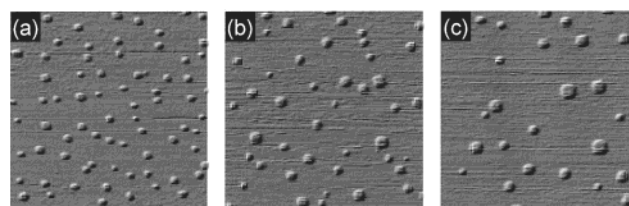


**Figure 5.** STM images ( $100 \times 100 \text{ nm}^2$ ) of the coarsening of Ag islands on Ag(100) with  $\theta \approx 0.015$  monolayer at times (a) 30 min; (b) 290 min; and (c) 470 min after deposition.

pathways which may control coarsening behavior.<sup>4</sup> For metal homoepitaxy, the traditional expectation is that coarsening should be dominated by Ostwald ripening.<sup>40</sup> However, we find that coarsening of Ag/Ag(100) adlayers at 295 K proceeds instead by diffusion and subsequent coalescence of large two-dimensional Ag islands.<sup>4,9,41</sup> We, and others, have termed this mechanism of coarsening “Smoluchowski ripening”.<sup>42,43</sup> This is the subject of the remainder of this section.

**4.2. Cluster Diffusion.** We were among the first to report diffusion of large, two-dimensional clusters, containing hundreds or even thousands of atoms, on metal surfaces.<sup>3</sup> For Ag(100), we found that a 100-atom cluster moves a distance of about 50 Å over a period of an hour. The diffusion of these large, flat clusters was surprising, not only because it violated an intuitive sense that metals are “static” at room temperature, but also because the ability of the cluster to remain intact during such a long-range displacement seemed almost biological. Nonetheless, theoretical work before and after our experimental observation pointed the way to understanding this phenomenon on an atomic scale, revealing several mechanisms by which such diffusion can occur.<sup>44–53</sup> These studies showed that the way in which the diffusion coefficient of a cluster varies with size can, in principle, reveal the mechanism by which such monsters migrate. We originally reported a diffusion coefficient which was invariant with size, suggesting that coarsening is controlled by attachment and detachment from island edges (evaporation–recondensation), thus randomly changing the position of the center of mass. However, our statistics were very limited, and later measurements by Pai et al. showed a strong dependence on size, suggesting that cluster diffusion is mediated by perimeter diffusion (PD), wherein atoms hop along the step edge, but do not detach and reattach.<sup>41,49–52,54</sup> A more recent simulation study<sup>9</sup> suggested that the dominant mass transport mechanism might actually be vacancy diffusion through the interior of the cluster. However, in these simulations, a very low activation barrier for vacancy diffusion was chosen, perhaps artificially enhancing this process. Regardless of the diffusion mechanism, however, the basic observation remains robust: Very large clusters on the (100) surfaces of soft metals—Ag, Cu, and presumably Au—move surprisingly quickly, even at room temperature.

**4.3. Coarsening Mechanism and Kinetics.** Subsequently, we investigated the mechanism of coarsening.<sup>4</sup> We did this by watching islands disappear with STM, as shown by Figure 5. When an island disappeared due to collision, we could clearly see another island in the immediate vicinity become larger as a result. However, for Ostwald ripening, the disappearance of a single island was accompanied by a minute (usually undetectable) increase in size of several surrounding islands. Using this criterion, we found that coarsening occurs mainly by the irreversible collision of diffusing clusters, at least at 295 K, on Ag(100). This result again contradicted the common wisdom of the time, but was subsequently confirmed in a different laboratory.<sup>41</sup>



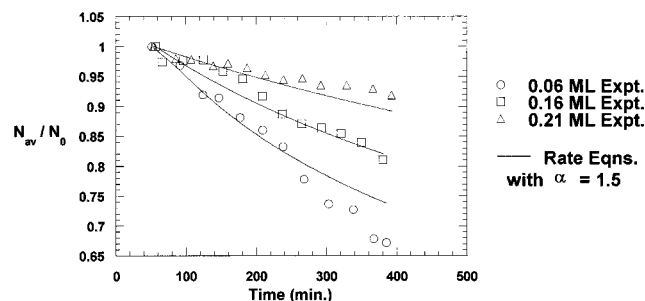


**Figure 6.**  $N_{av}/N_0$  versus  $t$  for  $\theta = 0.06, 0.16, 0.21$  monolayer, and initial island densities  $N_0 = 4.2 \times 10^{-4}, 4.7 \times 10^{-4}, 4.2 \times 10^{-4}$ /site, respectively. Reprinted with permission from ref 59. Copyright 1998 Elsevier Science.

In order to quantify the variation of cluster diffusivity,  $D(s) \approx D_0 s^{-\alpha}$ , with cluster size,  $s$ , we turned to the coarsening kinetics. The rate of coarsening should depend strongly on the mean island size, which controls the mean island diffusion coefficient,  $D_{av} \approx D(s_{av})$ . In addition, this rate should depend on the coverage, which controls the typical distance,  $L_{edge}$ , between island edges (i.e., the distance islands must diffuse before coalescing). One has that  $L_{edge} \approx (1 - \theta^{1/2})L_{av}$ , where  $L_{av} = (N_{av})^{-1/2}$  is the typical distance between island centers (in units of the lattice constant  $a$ ). Thus, the lifetime,  $\tau$ , of a typical island corresponds to the time to diffuse a distance  $L_{edge}$ , so it follows from Einstein's relation that  $(aL_{edge})^2 \approx 2 \times 4D_{av}\tau$ , the factor of 2 arising since the "target" island is also diffusing. Then, the mean-field rate equation for  $N_{av}$  becomes<sup>43</sup>

$$dN_{av}/dt \approx -N_{av}/\tau \approx -8a^{-2}D_0\theta^{-\alpha}(1 - \theta^{1/2})^{-2}(N_{av})^{2+\alpha} \quad (5)$$

so

$$N_{av} \approx [(N_0)^{-1-\alpha} + (1 + \alpha)At]^{-1/(1+\alpha)}$$

where  $A = 8a^{-2}D_0\theta^{-\alpha}(1 - \theta^{1/2})^{-2}$ , and  $N_0$  is the initial island density.<sup>35,36</sup> The latter result in (5) recovers the relation obtained in simulations of Smoluchowski ripening<sup>55–57</sup> for the temporal scaling exponent in terms of  $\alpha$ . Note that the above mean-field analysis ignores spatial correlations in the initial island distribution,<sup>18,19,23,24</sup> which would inhibit the initial coarsening.

We developed an effective method to assess or check the size dependence of cluster diffusivity, as follows: One measures the rate of coarsening for various initial island sizes at roughly constant separation.<sup>58</sup> We call these "tailored" studies, because of the deliberate control of size and separation. This control is achieved by depositing various coverages at roughly fixed  $F$ . Given that the coarsening mechanism is Smoluchowski ripening, a size-invariant cluster diffusion coefficient ( $\alpha = 0$ ) should mean that distributions of larger islands would coarsen more quickly than smaller islands, because their edges are closer (recall that the separation between island centers is roughly constant for fixed  $F$ ). However, for a diffusion coefficient that decreases strongly with cluster size ( $\alpha > 0$ ), one would have the opposite expectation: Distributions of larger islands would coarsen more slowly.

The experimental data for the coarsening kinetics is shown in Figure 6 for three coverages, 0.06, 0.16, and 0.21 monolayer, corresponding to initial island sizes of 140, 340, and 495 atoms, respectively. The kinetics slows with increasing island size, indicating  $\alpha > 0$ , consistent with the observations of Pai et al. The experimental data can be reasonably fit choosing  $\alpha \approx 1.5$  and  $D_0 \approx 1.75 \text{ Å}^2/\text{s}$ , with a substantial uncertainty in  $\alpha$  of around  $\pm 0.25$ . See refs 43 and 59 for further details.

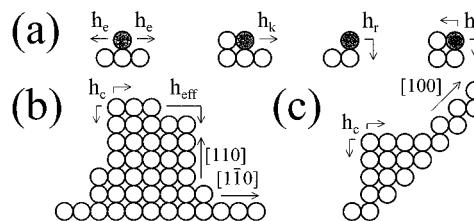


**Figure 7.** Schematic of (a) key perimeter diffusion processes (see text); (b) decay of protrusions at  $[1, -1, 0]$  (or equivalently  $[110]$ ) and  $[100]$  step edges. Reprinted with permission from ref 64. Copyright 1998 American Physical Society.

The above observations have consequences for experimental determination of the island size distribution immediately after deposition. As noted in section 2, it typically takes 15–30 min after deposition to obtain the first STM image on a large terrace from which size distributions are assessed. During this time, more rapid diffusion of the smaller clusters can significantly modify the shape of the size distribution (depleting the population of smaller islands). This likely explains the discrepancy between the observed and theoretical distributions noted in section 3.4.

The coarsening mechanism in a specific physical system may depend on feature size, separation, or temperature. We observed this for the Ag/Ag(100) system at 295 K, where Ostwald ripening occurs for extremely small or extremely far-separated islands.<sup>4</sup> For Cu/Cu(100), coarsening is reported to occur via cluster diffusion and coalescence at 295 K,<sup>41</sup> but via Ostwald ripening limited by attachment and detachment of vacancies at 340 K.<sup>8</sup>

## 5. Reshaping in the Submonolayer Regime

The collision and subsequent coalescence of clusters with other clusters, and with extended step edges, is an integral part of coarsening in the Ag/Ag(100) system at 295 K. But it is also an integral part of growth—islands in each layer collide as a result of growth during deposition, and their restructuring then influences subsequent growth in higher layers if it is significant on the time scale of deposition.<sup>60,61</sup> In addition, analysis of restructuring can provide fundamental insight into atomic motion at step edges (cf. Figure 8a). Many studies have pursued the latter goal, but their focus has usually been on "perfect" extended step edges undergoing near-equilibrium fluctuations.<sup>62</sup> However, it might be more desirable to monitor decay of far-from-equilibrium configurations than fluctuations about an equilibrium configuration, because the former evolve far more dramatically than the latter. The difference is analogous to the difference between studying geological erosion on a mountainside or on a plain. Naturally, the former yields richer information, and at a faster rate.

Below, we focus on two orientations for extended step edges. The close-packed step orientation, the  $[110]$ , is the equilibrium orientation. The open, metastable  $[100]$  orientation (and other nonequilibrium orientations) can exist on the clean surface because of step pinning,<sup>63</sup> or on the growth surface because of island coalescence. The atomic structure of these steps is shown in Figure 7b,c.

**5.1. Experimental Observations at 295 K.** Here, we consider four distinct types of events:<sup>64</sup> collision of clusters with extended step edges which are (a) close-packed, and (b) open; (c) side-to-side, and (d) corner-to-corner collision of pairs of square clusters. Figure 8 provides an illustration of each of these events from STM. When an island collides with a step, it always merges with the step and disappears. When an island collides



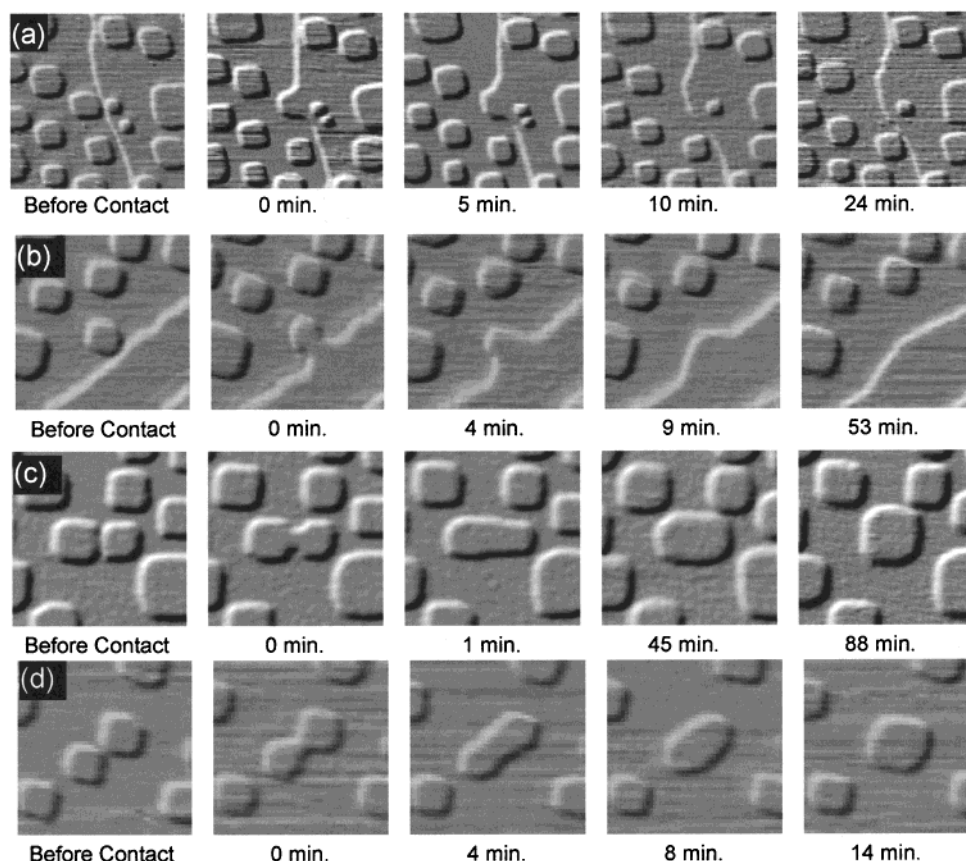


**Figure 8.** STM images of coalescence of (a) a cluster and a [110] step (image =  $56 \times 56 \text{ nm}^2$ ); (b) a cluster and a [100] step ( $40 \times 40 \text{ nm}^2$ ); (c) a side-to-side cluster pair ( $28 \times 28 \text{ nm}^2$ ); and (d) a corner-to-corner cluster pair ( $50 \times 50 \text{ nm}^2$ ).

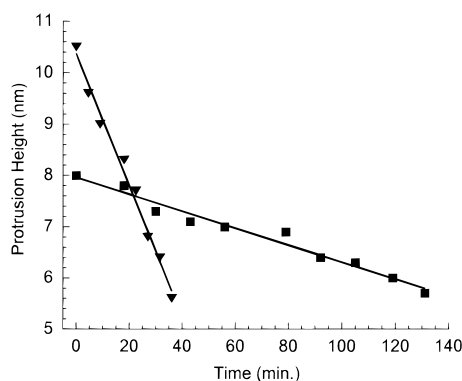


**Figure 9.** Comparison of the decay of the heights of a square protrusion of area  $140 \text{ nm}^2$  on the [001] step edge (shown as inverted triangles), and a triangular protrusion of area  $130 \text{ nm}^2$  on the [011] step edge (shown as squares). The solid lines are meant only as a guide for the eye.

with another island, the two always evolve toward a single square shape. In both cases, the final state minimizes the step edge free energy, within the constraints imposed by the more global system (e.g., an extended step itself cannot change average orientation).

In most of these cases, we find that some simple geometrical quantity (e.g., height of the bump, width of the neck) varies linearly with time over a substantial regime, thus allowing the *rate* of restructuring to be defined as the slope of the line. Two such examples are shown in Figure 9. This is convenient for comparison between simulation and experiment. In such comparisons, we have focused on the variation of rate with island size, so many situations such as those shown in Figure 8 have been analyzed and also simulated, as described below. See also Table 3.

We now describe in detail some features of the experimental observations. When an island collides side-on with a close-packed [110] step edge (Figure 8a), the step remains smooth and the island continuously evolves into a rounded bump or protrusion and then disappears. Experimental data for colliding islands, and thus protrusions ranging from  $15 \times 15$  to  $60 \times 60$  atoms reveal that the rate of decay of the height of the protrusion satisfies  $R \approx 550A^{-1}$  lattice constants/min, for the early stage of decay, with island or protrusion area  $A$  measured in units of atoms. See Table 3. When an island touches corner-on to an open [100] step edge, it quickly forms a meniscus-like neck (Figure 8b), accompanied by large indentations or depressions (facets) in the step edge. The facets show immediately that there must be mass flow from the step edge into the neck, at least in this stage. Eventually, the neck broadens and the protrusion adopts a triangular shape at the step, which then melts slowly into the step. For the decay of height of a triangular protrusion, there is significant scatter in the experimental data, but we estimate that  $R \approx 250A^{-1}$  lattice constants/min.

Two islands of unequal size colliding side-on behave as in Figure 8c: they first “equalize” quickly, by adopting an overall rectangular shape (which is metastable), then much more slowly contract into a square. Two islands approaching corner-to-corner (Figure 8d), somewhat analogous to an island approaching a [100] step edge, also form a meniscus-like neck, then merge into an amoeba-like shape, and finally become a square. Our data show that the rate of growth of the neck width is described by  $G \approx 1300A^{-1}$  lattice constants/min, where  $A$  is the area of each island (see Table 3).

One interesting observation is that, for equally-sized islands, the rate of decay of the triangle along the open step edge is substantially slower than the rate of decay of the bump along

**TABLE 3: Initial Decay Rates (in lattice constants/min) for Square Protrusions at [110] Step Edges, and Neck Growth Rates (in lattice constants/min) for Corner-to-Corner Collision of Roughly Equal-Sized Square Islands**

protrusion area	295 atoms	506 atoms	852 atoms	992 atoms	1500 atoms	1620 atoms
height decay: expt	1.28	1.06	0.62	0.55	0.47	0.42
height decay: sim	1.54	0.99	0.62	0.54	0.37	0.36
indiv island area	361 atoms	510 atoms	825 atoms	2055 atoms	2500 atoms	4505 atoms
neck growth: expt	4.17	2.21	2.02	0.53	0.56	0.20
neck growth: sim	3.79	2.50	1.43	0.53	0.43	0.23

the close-packed step edge, especially for large sizes  $A$ . This is shown in Figure 9. On the basis of the following arguments, this suggests that the reshaping is dominated by adatom diffusion *along* the step or island edge, rather than by attachment–detachment processes. From Figure 9, one sees intuitively that adatom diffusion is expected to be much slower along the open step edge than along the close-packed step edge. (We caution, however, that the barrier for diffusion along a perfect [100] step edge may actually be lower than that chosen in the modeling discussed below.) This, plus the fact that cluster diffusion was found to occur primarily by atomic motion around the periphery (section 4.3), leads us to postulate that the primary reshaping mechanism is atomic motion along the step and island edges. Thus, this is a primary assumption in our KMC simulations of reshaping.

Another interesting comparison is between the growth of the meniscus-like neck formed when a cluster collides with a [100] step edge, and that formed when two roughly equal sized clusters collide corner-to-corner. In both cases, there is a rapid initial increase in the neck width followed by a more sustained period of quasi-linear increase which can be characterized by a single growth rate as listed in Table 3. For the island-to-step case, the growth rate is roughly an order of magnitude *larger* than for the island-to-island case. This is due to the above-mentioned formation of large indentations in the [100] step edge (whose sides have preferred [110] or  $[1, -1, 0]$  orientations; cf. Figure 8b), and the associated rapid flow of mass to the neck. Mass can be drawn from any location along the step edge including those close to the neck. This contrasts the corner-to-corner case where mass must at least initially come from the more distant and localized corners of the clusters.

Finally, we have also considered restructuring of the “mirror image” structures to those above, i.e., vacancy indentations in extended step edges, and rectangular and dumbbell shaped vacancy clusters. The latter is significant for our discussion in sections 6 and 7 below. Restructuring rates appear similar to those for adatom protrusions and clusters of the same size.

**5.2. Theoretical Analysis.** Analysis of the relaxation dynamics rests on key assumptions about the underlying atomistic perimeter diffusion processes, and of their energetics. The key processes shown in Figure 7a include the following: fast edge diffusion along straight [110] steps at rate  $h_e$ ; kink escape at rate  $h_k$ ; corner rounding at rate  $h_r$ ; and slow “core breakup” at rate  $h_c$ . Corresponding activation barriers are denoted by  $E_i$  ( $i = e, k, r, \text{ or } c$ ), and we assume a common attempt frequency,  $\nu = 10^{12}/\text{s}$ . We also model the system with effective nearest-neighbor (NN) pairwise adatom interactions of magnitude  $J$ . Then, the detailed-balance relationship between rates for forward and reverse processes implies that  $h_k/h_e = h_r/h_e = \exp[-J/(k_B T)]$ . Semiempirical energy calculations for metal(100) homoepitaxy<sup>46,65</sup> suggest that  $h_r \approx h_k$ , so we choose  $E_r \approx E_k = E_e + J$ , and  $E_c \approx E_e + 2J$ .

At this point, we are left with two adjustable parameters in the KMC model:  $E_e$  and  $J$ . For Ag/Ag(100) homoepitaxy, calculations show that a reasonable expectation is that  $E_e \approx$

$E_d/2$ .<sup>26,27,46</sup> Since we know  $E_d = 0.4$  eV from the growth kinetics (section 3.3), we set  $E_e \approx 0.2$  eV. Hence, we are able to reduce the number of adjustable parameters to one,  $J$ . This presents a rather stringent challenge to the simulations: They must match experiments over a range of experimental geometries (Figure 8) and island areas, with a single value of  $J$ .

The KMC simulations do in fact match the experimental data well with a single value of  $J$ . First, we consider the rate of decay,  $R$ , of the height of protrusions at extended step edges as a function of the area,  $A$ , of the protrusion. This behavior is matched by simulations with  $E_e = 0.20$  eV, and an effective nearest-neighbor interaction of  $J = 0.28$  eV. The decay of height of a triangular protrusion following collision of an island with an [100]-type step is matched reasonably by the same value of  $J$  (noting the large experimental uncertainties). For the corner-to-corner collision of two islands, growth of the width of the meniscus-like neck is matched remarkably well by simulations with the same value of  $J$ . Hence, the model seems consistent with the data and yields a single value of  $J$ .

One quantity of primary interest is the effective activation barrier,  $E_{\text{act}}(\text{PD})$ , for the overall step-edge restructuring process. Consider the decay of the square protrusion on a [110] step edge shown in Figure 8a. At various stages, it is necessary to disrupt the “rectangular core” of the protrusion via “core breakup”. In addition, reduction of the height of the protrusion requires a repeated combination of kink escape and corner rounding. See Figure 7b. Careful analysis shows that the effective barrier for the combined process corresponds to that for core breakup.<sup>64</sup> Thus, the effective barrier for protrusion decay is  $E_{\text{act}}(\text{PD}) \approx E_e + 2J$ . This value of the effective barrier will also apply for the other PD-mediated restructuring processes considered here. Finally, it is appropriate to consider the competing pathway for mass transport via detachment and reattachment (evaporation–recondensation, EC) of atoms from the step edge. The effective barrier for evaporation, and thus for mass transport, would be  $E_{\text{act}}(\text{EC}) = E_d + 2J$ .<sup>64</sup> Substituting the values into the equations for  $E_{\text{act}}(\text{PD})$  and  $E_{\text{act}}(\text{EC})$  shows that that PD should have a significant energetic advantage of 0.2 eV over EC. Thus, PD should indeed dominate, at least for smaller-size features, and lower temperatures, consistent with our modeling.

## 6. Growth and Kinetic Roughening in the Multilayer Regime

**6.1. Background.** A detailed understanding and characterization of multilayer growth during deposition, even for simple metal(100) homoepitaxial systems, is a surprisingly recent development.<sup>20,66</sup> It is based on the observation of Villain<sup>66</sup> that a step-edge barrier<sup>67,68</sup> inhibiting downward transport (relative to terrace diffusion) produces a lateral mass current in the uphill direction. This results in growth instability leading to “mound” formation. Because of this and other recent insights into the atomistic details controlling multilayer growth for metal(100) homoepitaxy, often our models have quantitative predictivity<sup>20</sup>!

The step-edge barrier in metal(100) homoepitaxy is often small, resulting in initial quasi-layer-by-layer growth, as was evident in section 3. We note that for ideal layer-by-layer growth, various parameters, such as the roughness, should oscillate indefinitely as the film grows. One experimental signature of such growth is the appearance of persistent oscillations in the intensities of surface-sensitive diffraction probes. These are often observed for metal(100) homoepitaxy, but even here one finds eventual decay of the oscillations signaling kinetic roughening of the growing film.<sup>20</sup>

We first introduce the basic quantities characterizing multilayer film structure.<sup>69</sup> We label layers by an index  $j = 0, 1, 2, \dots$ , with  $j = 0$  denoting the substrate. Let  $\theta_j$  denote the coverage of layer  $j$  (so  $\theta_0 = 1$  and  $\theta = \sum_{j \geq 1} \theta_j$ ). Then, the fraction of exposed atoms in layer  $j$  is given by  $P_j = \theta_j - \theta_{j+1}$ , where  $\sum_{j \geq 0} P_j = 1$  and  $\sum_{j \geq 0} jP_j = j_{\text{av}} = \theta$ . Two key quantities characterizing the film height distribution are its (interface) width,  $W$ , which gives a measure of film roughness, and its skewness,  $\kappa$ , which gives a measure of the deviation from a symmetric height distribution. These quantities satisfy

$$W^2 = \sum_{j \geq 0} (j - j_{\text{av}})^2 P_j$$

$$\kappa = \sum_{j \geq 0} (j - j_{\text{av}})^3 P_j / W^3 \quad (6)$$

After any initial oscillations in  $W$  have dissipated, kinetic roughening is characterized by the behavior  $W \sim c\theta^\beta$ , with nontrivial exponent  $\beta$ .

The kinematic diffracted intensity is determined by the film height-difference distributions,  $G_n(r)$ , for finding surface atoms separated laterally by  $r$ , with a height difference  $n = 0, \pm 1, \dots$  layers. Traditional analyses have assumed Gaussian height and height-difference distributions in developing expressions for the Bragg intensity,  $I_{\text{Bragg}}$ , and the diffuse intensity,  $I_{\text{diff}}$ .<sup>70</sup> However, we find that these conditions are not satisfied for mounded film morphologies of relevance here, and have thus developed a more general theory.<sup>60,61</sup> Here, we just note that at the antiphase condition, the diffracted intensity for lateral momentum transfer  $q$  has the general form<sup>60,61</sup>

$$I(q, q_z) \propto (2\pi)^2 I_{\text{Bragg}} \delta(q) + I_{\text{diff}}(q) \quad (7)$$

$$I_{\text{Bragg}} \approx 4 \cos^2[\pi\theta - \kappa\pi^3 W^3/3!] \exp[-\pi^2 W^2]$$

where  $\delta$  denotes the Dirac delta function. This theory reveals a characteristic oscillatory decay of the Bragg oscillations with minima shifted from half-monolayers for skewness  $\kappa \neq 0$ . The form of the diffuse intensity is controlled by  $W$ , as well as by the Fourier transform of the shape of the height-difference distribution,  $G_n(r)$ . Our results show that the initial ring structure of  $I_{\text{diff}}$  (discussed in section 3) should be washed out as the film roughens, or more specifically as  $q_z W$  becomes larger.<sup>60,61</sup>

In the analysis of experimental data below, we build upon the “canonical” KMC simulations developed in section 3 for the irreversible formation of near-square islands.<sup>60,61</sup> In order for them to be applicable in the multilayer regime, the model is extended as follows. First, atoms landing on top of islands diffuse at the same rate as on the substrate. Second, they can nucleate within the same layer or aggregate with higher layer islands, just as in the submonolayer regime. Third, they can diffuse to island edges and hop down at reduced rate  $h' = h \exp[-E_{\text{Sch}}/(k_B T)]$ , where  $E_{\text{Sch}}$  denotes the step-edge barrier. Finally, for multilayer growth, it is important to specify that

atoms which do not deposit directly at 4-fold hollow (4FH) sites, but rather at island edges or on top of microprotrusions, funnel down until they reach a lower 4FH site.<sup>12</sup> We shall see below that this funneling process plays a key role in the determination of multilayer structure, even for large islands.

**6.2. Initial Stages of Multilayer Growth and Step-Edge Barrier Estimation.** Deviations from layer-by-layer growth are most apparent around monolayer coverages, so analysis of the film morphology at such coverages should provide the most precise estimates of the step-edge barrier.<sup>5,6</sup> Consequently, we deposited about 1 monolayer of Ag on Ag(100) at 295 K, with  $F \approx 0.055$  monolayer/s. We estimated that, immediately after deposition,  $\theta_1 \approx 0.940$  monolayer,  $\theta_2 \approx 0.057$  monolayer, and  $\theta_j = 0$ , for  $j \geq 3$  (within  $\pm 0.005$  monolayer). In the KMC simulations, we assumed irreversible island formation and  $E_d = 0.38$  eV (because both were demonstrably true for submonolayer growth; cf. section 3). The only remaining free parameter,  $E_{\text{Sch}}$ , was adjusted to match the observed layer coverages after deposition of 1 monolayer of Ag. The results indicate that  $E_{\text{Sch}} \approx 25$  meV (but one could instead set  $E_{\text{Sch}} = 0$  and reduce the attempt frequency for  $h'$  relative to  $h$ ).<sup>5,6</sup> For comparison, the current best high-level calculation yields an estimate of  $E_{\text{Sch}} = 0 \pm 50$  meV for [110] step edges.<sup>26,27</sup> We emphasize the small nonzero value of  $E_{\text{Sch}}$  has a profound effect on multilayer growth (see section 6.3).

There are some sources of uncertainty in our estimate and interpretation of  $E_{\text{Sch}}$  (apart from assuming a common  $\nu$  for all hopping processes). First, our modeling does not incorporate possible restructuring of growing islands upon coalescence to form larger squares (cf. section 5.1). Rather, they continue growing as overlapping squares. Such restructuring would effectively inhibit downward transport by increasing the mean size of individual islands, and if included in the model produces a substantially lower estimate for  $E_{\text{Sch}}$ .<sup>60,61</sup> Second, it has been noted that the potential energy surface felt by an atom diffusing on top of an island can be nonuniform, e.g., exhibiting a weak attractive well near island edges, in addition to a repulsive barrier right at the step edge.<sup>71</sup> In such a case,  $E_d + E_{\text{Sch}}$  should be interpreted as the height of the repulsive barrier right at the step edge measured relative to a potential well in the center of the island. Third, the step-edge barrier around the island perimeter could be quite different at kink sites or corners, than along straight edges. To reasonably model such variations in  $E_{\text{Sch}}$  would require a more sophisticated treatment of island edge diffusion and associated shape fluctuations. Thus, our estimate of  $E_{\text{Sch}}$  should be regarded only as an *effective* barrier, i.e., a value which serves to match the KMC model with experiment.

**6.3. Kinetic Roughening in Thick Multilayer Films.** Since all the parameters have now been determined in our model for Ag/Ag(100) homoepitaxy, we can examine its predictions for the kinetic roughening and morphology of thick films. For example, our KMC simulations show that kinetic roughening is described by an effective exponent of  $\beta \approx 0.20$ , for the regime of 10–20 monolayers with  $F \approx 0.055$  monolayer/s at 295 K. The skewness is negative and increases in magnitude with thickness. The result for  $\beta$  is consistent with the experimental observations of refs 72 and 73. Figure 10a shows the corresponding increase of  $W$  with  $\theta$ , and the decay of the Bragg oscillations at the antiphase condition. Figure 10b shows a snapshot of the simulated film morphology at 100 monolayers.

In section 6.1, we noted the observation of Villain<sup>66</sup> that the presence of a step-edge barrier leads to biased reflection of atoms from descending steps, and incorporation at ascending steps, which produces a lateral mass current in the uphill



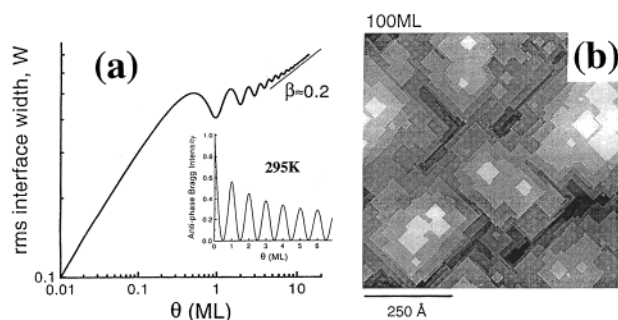


**Figure 10.** Multilayer growth of Ag/Ag(100) at 295 K with  $F = 0.06$  monolayer/s. Predictions of simulation with  $E_d = 0.38$  eV and  $E_{\text{Sch}} = 25$  meV for (a)  $W$  versus  $\theta$ ; the inset shows  $I_{\text{Bragg}}$  versus  $\theta$  at the out-of-phase condition; (b) the morphology of a 100 monolayer Ag/Ag(100) film.

direction. This produces unstable growth characterized by the formation of mounds. Various dynamic or equilibrating processes can produce a downhill current, and the typical mound slope then increases until there is a balance between uphill and downhill currents. For metal(100) homoepitaxy with irreversible island formation, a downhill current is produced by downward funneling of atoms deposited at step edges and at microperturbations to lower 4FH sites.<sup>12</sup> This leads to selection of mound slopes, and also strongly influences roughening.<sup>60,61</sup> For Ag/Ag(100) homoepitaxy, we find a selected mound slope at 295 K of about  $6^\circ$  for  $F \approx 0.06$  monolayer/s.<sup>74</sup> Thus, the mounds are rather flat and broad, as is apparent from Figure 10b.

We can also predict the temperature dependence of growth. As is generally the case for metal(100) homoepitaxy, we find that the roughness,  $W$ , and the “effective”  $\beta$  vary significantly with  $T$ .<sup>60,61,74</sup> Due to the increased difficulty in surmounting the step-edge barrier, at first the film becomes progressively rougher as  $T$  decreases below 295 K. In particular, we find that  $\beta \approx 0.3$  for 10–20 monolayer films at 200 K, again consistent with experimental observations.<sup>72,73</sup> But, at lower temperatures, the film becomes smooth again, reflecting the increased influence of downward funneling due to the higher step density.<sup>60,61</sup> In contrast, the step density increases monotonically with decreasing  $T$ . In reality, downward funneling is not always operative. An atom depositing on the (111) facet corresponding to the side of a large steep pyramid will not always funnel to the bottom. However, the barrier for diffusion on such facets is very low (0.1 eV), so typically the atom can diffuse to the bottom anyway (mimicking perfect funneling). However, at very low  $T$ , even such “easy diffusion” is inoperative, and the breakdown of downward funneling can lead to formation of overhangs and defects.<sup>75–77</sup> Rough growth can reappear!

A comprehensive set of experimental data for the mound slope and roughness over a broad range of temperatures below room temperature is not yet available. Some piecemeal evidence is available from other groups, and is consistent with the model, as noted above.<sup>11,72,73,78</sup> Additionally, we have tested part of the model ourselves using HRLEED. The simulation suggests that kinetic roughening during Ag/Ag(100) homoepitaxy, and thus changes in the HRLEED profiles, should be more dramatic for temperatures closer to 200 K than to 300 K. Thus, we have performed HRLEED studies of multilayer growth at 220 K for incremental 1 monolayer depositions up to 27 monolayers.<sup>79</sup> The diffraction profile evolution during growth measured at the out-of-phase condition is shown in Figure 11. Visual inspection reveals that after subtracting the central Bragg peak, the remaining diffuse profile evolves from a split “ring” structure to a monomodal profile during growth, as expected from

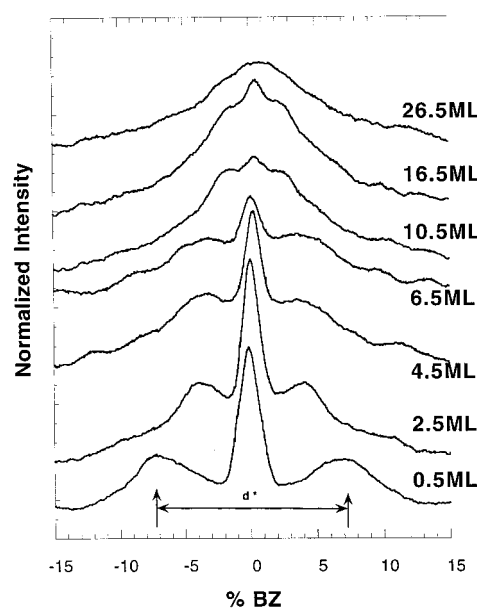


**Figure 11.** Diffraction profiles at the out-of-phase condition for deposition of Ag on Ag(100) at 295 K with  $F \approx 0.002$  monolayer/s. Profiles for various coverages up to 26.5 monolayers are shown, and the diameter,  $d^*$ , of the ring is indicated for 0.5 monolayer.

theory.<sup>60,61</sup> Furthermore, before it disappears, the diameter of the ring satisfies the relation  $d^* \propto \theta^{-0.3}$ , implying that the lateral mound dimension,  $L_m$ , satisfies  $L_m \propto 1/d^* \propto \theta^{0.3}$ . Given the above prediction for  $W \propto \theta^{0.3}$ , this implies that  $W \propto L_m$ , corresponding to (rapid) slope selection. However, experiments involving direct (nonincremental) deposition of multilayer films<sup>79</sup> indicate slower coarsening, with  $L_m \propto \theta^{0.2}$ , which implies that mound slope increases as  $W/L_m$  at least up to 25 monolayers.

We have also shown that for a rough film at 20 monolayers, where the split diffraction profile is lost at the out-of-phase condition, if one reduces  $q_z$  toward the in phase condition, then splitting is recovered.<sup>79</sup> This feature is expected from the theory<sup>60,61</sup> which shows that the profile shape is controlled by the combination  $q_z W$ , as has been discussed by Yang et al.<sup>80</sup>

Finally, we note that analogous kinetic roughening, mound coarsening, and associated diffraction profile evolution, has been observed in Fe/Fe(100)<sup>81</sup> and Cu/Cu(100)<sup>82,83</sup> homoepitaxy.

## 7. Smoothing (Reshaping) of Multilayer Films

As noted in the Introduction, multilayer films will relax to their smooth equilibrium structure after deposition. First, we consider this process for the same situation described in section 6.2, the barely rough multilayer formed by 1 monolayer of Ag on Ag(100) at 295 K. In Figure 12a, we show the prediction from simulations of our multilayer growth model for the film structure immediately after deposition of 1 monolayer with  $F \approx 0.06$  monolayer/s at 295 K. Figure 12b,c shows STM images for film structure 46 min and 139 min after deposition under these conditions. Monitoring film evolution for several hours reveals a slow decrease in the second layer coverage,  $\theta_2$ , from its initial value of about 0.06 monolayer (see Figure 12), matched exactly by an increase in the first layer coverage,  $\theta_1$  (reflecting mass conservation). There is initially a much stronger decrease in the density,  $N_{\text{second}}$ , of second layer adatom islands from about  $9 \times 10^{-5}$  to  $2.2 \times 10^{-5} \text{ \AA}^{-2}$  after 46 min. Subsequently, the decrease in  $N_{\text{second}}$  is slower, more closely matching that of  $\theta_2$ , such that the mean island size,  $s_{\text{av2}} = \theta_2/N_{\text{second}}$ , remains roughly constant, for a few hours, before slowly decreasing. See Table 4. One also observes the rapid restructur-

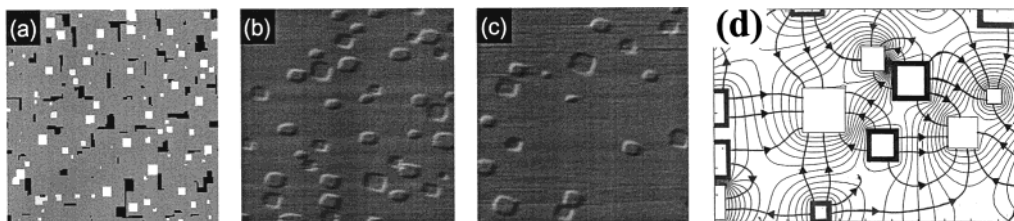


**Figure 12.** Configurations of 1 monolayer Ag/Ag(100) films ( $100 \times 100 \text{ nm}^2$ ) grown at 295 K with  $F = 0.06$  monolayer/s: (a) immediately after deposition (from simulation), where white (black) regions denote second layer islands (first layer vacancies); Reprinted with permission from ref 6. Copyright 1998 Elsevier Science. (b) 45 min, and (c) 139 min after deposition (from experiment). (d) Solution of the Laplace equation for the steady-state density (thin contour lines) of diffusing second layer adatoms in a region corresponding to the bottom right portion of the experimental film configuration (b). Edges of second layer square islands are shown by thick lines, and of first layer square vacancies by thin lines. The curves with arrows indicate the diffusive flux lines.

**TABLE 4: Postdeposition Smoothing of a 1 monolayer Ag/Ag(100) Film at 295 K<sup>a</sup>**

time (min)	$\theta_1$	$\theta_2$	$N_{\text{second}}$	$S_{\text{av2}}$
46	0.950	0.051	$2.24 \times 10^{-5}$	2240
88	0.954	0.042	$1.90 \times 10^{-5}$	2210
123	0.958	0.035	$1.51 \times 10^{-5}$	2310
185	0.973	0.028	$1.35 \times 10^{-5}$	2070
250	0.973	0.021	$1.11 \times 10^{-5}$	1890
437	0.983	0.010	$0.61 \times 10^{-5}$	1640

<sup>a</sup> Here  $\theta_i$  are layer coverages,  $N_{\text{second}}$  is the second layer island density (per  $\text{\AA}^2$ ), and  $S_{\text{av2}} = \theta_2/N_{\text{second}}$  (in  $\text{\AA}^{-2}$ ).

ing of vacancies in the first layer from highly irregular shapes immediately after deposition to achieve compact shapes (cf. section 5.1).

The island dynamics underlying these changes are rather complex. The second layer island array evolves via a combination of dissolution (as for smaller islands during Ostwald ripening), and cluster diffusion with occasional coalescence. An enhanced driving force for dissolution (compared with the same island distribution on the substrate) is provided by the “adatom sinks” at the edge of the first layer vacancy islands. The preferred dissolution of smaller islands, particularly those close to vacancies, tends to keep the average island size,  $s_{\text{av2}}$ , roughly constant, and is presumably responsible for the initial rapid decrease in island density. Throughout the film evolution, first layer vacancies tend to be filled by mass transport from the second layer, but appear to simultaneously undergo coarsening, maintaining their average size. We have observed such vacancy-island coarsening previously (in the absence of second layer islands), and attributed it almost exclusively to Ostwald ripening.<sup>4</sup> Vacancy islands diffuse somewhat more slowly than their mirror-symmetry adatom islands in this system, which inhibits Smoluchowski ripening relative to Ostwald ripening.<sup>4</sup>

It is natural to attempt to quantify the rates of decay of individual second layer islands, and of filling of individual vacancies, as well as the overall rate of mass transport to the first layer. For the simplest treatment, one solves the Laplace equation,  $\partial N_1/\partial t \approx D_{\text{ter}} \nabla^2 N_1 = 0$ , for the steady-state density of diffusing second layer adatoms, which detach from and reattach to second layer island edges (there is no additional barrier to attachment), and which are trapped at the edges of first layer vacancies (after overcoming the step-edge barrier). To this end, we adapt a formalism applied by the Jülich group to analyze the decay of Cu islands on Cu(111) in the presence of step edges.<sup>84</sup>

One assumes that the density of adatoms at the edge of second layer islands of “radius”  $R$  is determined by the quasi-equilibrium Gibbs–Thompson equation

$$N_1 \approx N_{\text{eq}+}(R) \approx N_{\text{eq}}(\infty) \exp[+\alpha\beta^{[110]}/(Rk_{\text{B}}T)] \quad (8)$$

where  $N_{\text{eq}}(\infty)$  is the equilibrium adatom density on an island free terrace,  $\beta^{[110]} \approx 0.13 \text{ eV/atom}$  is the [110] step edge free energy,<sup>26,27</sup> and  $\alpha$  is a geometrical factor of order unity.<sup>8,84</sup> At the edge of vacancy islands with “radius”  $R$ , if  $n$  is the outward normal to the edge, one has

$$\underline{n} \cdot dN_1/d\underline{r} = [N_1 - N_{\text{eq}}(R)]/L_{\text{Sch}} \quad (9)$$

Here  $N_{\text{eq}}(R)$  is the quasi-equilibrium adatom density at the edge of vacancy islands, which is given by (8) but with a change of sign in the exponent. (This reflects the opposite sign curvature of the edges of vacancy and adatom islands.) Also  $L_{\text{Sch}} \approx a \exp[E_{\text{Sch}}/(k_{\text{B}}T)]$  is the “Schwoebel length” which reflects the magnitude of the step-edge barrier.<sup>85,86</sup> We anticipate that for Ag/Ag(100) at 295 K, the step-edge barrier will not significantly hinder interlayer transport since  $L_{\text{Sch}}$  ( $\approx 2.7$  atoms at 295 K) is much smaller than the characteristic sizes and separations of islands and vacancies. Thus, we replace (9) by  $N_1 \approx N_{\text{eq}}(R)$ . In Figure 12d, we show the numerical solution of this complex diffusion problem at 295 K for a portion of the experimental distribution of islands and vacancies in Figure 12b.

Turning now to thicker multilayers, there are several STM studies of relaxation of films in the few monolayer range,<sup>87,88</sup> but very little investigation in the regime of dozens of monolayers. For the mean terrace width,  $L_{\text{terr}}$ , one expects temporal scaling of the form  $L_{\text{terr}} \sim t^x$ , with  $x$  dependent on the driving force governing mass transport in the smoothing kinetics.<sup>89</sup> For the initial multilayer island stacks, the driving force is likely the line tension of curved step edges and  $x = 1/3$ , but a transition to a different mechanism and scaling is possible for later times (characterized by larger  $L_{\text{terr}}$  and smaller step curvatures). Indeed, these features were observed in the smoothing of 100 monolayers Cu/Cu(100) films created by deposition at 0.7 monolayer/min and at 295 K.<sup>90</sup> Monomodal HRLEED profiles taken at the out-of-phase condition were used to assess the terrace width evolution. One expects similar behavior for thick Ag/Ag(100) films. To date, the only experiments have been with 20 monolayers films deposited at 220 K using HRLEED closer to the in-phase condition where the profiles are still split. Some evolution of the ring profile was observed over a few hours at 220 K.<sup>79</sup>

## 8. Summary

There have been a number of results from our work, which could not have been anticipated at the outset. First is the realization that the shape of the island size distribution can be expressed explicitly in terms of the island size dependence of the capture numbers, basic quantities describing the growth rate of islands. Furthermore, this dependence of capture numbers on island size has a straightforward geometric interpretation,

but it is very different from accepted mean-field predictions. Second is the diffusion of large pancake-like clusters, and the fact that this diffusion is the predominant mechanism of coarsening. Third is the fact that simple qualitative observations of cluster reshaping provide insight into the mechanism governing the process, and that this reshaping can be modeled quantitatively for a variety of geometries using only a single adjustable parameter. Fourth is the prediction, from the KMC simulations, that films should become smooth at lower temperatures where terrace diffusion is inoperative, simply due to the influence of downward funneling. These results have provided significant insight into the general or global view of film growth.

Our effort to extract information about key energetic barriers and atomic-scale mechanisms has been fruitful. It is encouraging to note the synergism between information derived from the various types of phenomena: That is, parameters and mechanisms derived for one type of process are consistent with or have provided key input for another. As an example, the single-atom terrace diffusion barrier, derived from submonolayer growth studies, is used for multilayer growth, and also to provide insight into mass transport at step edges which controls restructuring. Bond energies extracted from modeling the transition to reversible island formation are consistent with those used in analysis of step edge restructuring. Another example: the observation that perimeter diffusion is the mechanism of cluster diffusion allows us to reasonably postulate that this is the mechanism of cluster reshaping as well. Yet another sort of feedback comes from the cluster diffusion and two-dimensional reshaping kinetics. In principle, one could (and should) now incorporate these processes realistically during growth, although we have not yet done so. The interesting point is that a self-consistent picture has developed of the atomic-scale processes, and that this picture appears to explain widely different phenomena in Ag(100) homoepitaxy.

Virtually all of the insights obtained in this work for the simple Ag/Ag(100) system, whether they relate to submonolayer nucleation and growth, multilayer kinetic roughening, or post-deposition relaxation processes, are directly applicable to a broad variety of more complicated and technologically relevant systems. These include heteroepitaxial metal films of relevance to magnetic and catalytic technologies. Likewise, all the above processes apply to semiconductor (as well as metal) thin films. From this perspective, there is substantial potential payoff from our comprehensive analysis of what might seem to have been a simple and well understood system.

**Acknowledgment.** This work was supported by NSF Grant CHE-9700592. It was performed at Ames Laboratory which is operated for the USDOE by Iowa State University (ISU) under Contract No. W-7405-Eng-82. We also acknowledge support from IPRT (ISU). Experiments described here were performed by Conrad Stoldt, Laurent Bardotti, Luke Chang, Cynthia Jenks, Tony Layson, Jianming Wen, and Chenming Zhang, and Monte Carlo simulations were performed by Maria Bartelt and Antonio Cadilhe. We thank them all. Conrad Stoldt deserves special acknowledgment for preparing many of the figures.

## References and Notes

- (1) Kalff, M.; Comsa, G.; Michely, T. *Phys. Rev. Lett.* **1998**, *81*, 1255.
- (2) Hannon, J. B.; Bartelt, M. C.; Bartelt, N. C.; Kellogg, G. L. *Phys. Rev. Lett.* **1998**, *81*, 4676–4679.
- (3) Wen, J.-M.; Burnett, J. W.; Chang, S.-L.; Evans, J. W.; Thiel, P. A. *Phys. Rev. Lett.* **1994**, *73*, 2591.
- (4) Wen, J.-M.; Evans, J. W.; Bartelt, M. C.; Burnett, J.; Thiel, P. A. *Phys. Rev. Lett.* **1996**, *76*, 652.
- (5) Zhang, C.-M.; Bartelt, M. C.; Wen, J.-M.; Jenks, C. J.; Evans, J. W.; Thiel, P. A. *J. Crystal Growth* **1997**, *174*, 851–857.
- (6) Zhang, C.-M.; Bartelt, M. C.; Wen, J.-M.; Jenks, C. J.; Evans, J. W.; Thiel, P. A. *Surf. Sci.* **1998**, *406*, 178–193.
- (7) Bardotti, L.; Stoldt, C. R.; Jenks, C. J.; Bartelt, M. C.; Evans, J. W.; Thiel, P. A. *Phys. Rev. B* **1998**, *57*, 12544.
- (8) Hannon, J. B.; Klücker, C.; Giesen, M.; Ibach, H.; Bartelt, N. C.; Hamilton, J. C. *Phys. Rev. Lett.* **1997**, *79*, 2506–2509.
- (9) Heinonen, J.; Koponen, I.; Merikoski, J.; Ala-Nissila, T. *Phys. Rev. Lett.* **1999**, *82*, 2733.
- (10) Costantini, G.; Rusponi, S.; Gianotti, R.; Boragno, C.; Valbusa, U. *Surf. Sci.* **1998**, *416*, 245–254.
- (11) Egelhoff, W. F.; Jacob, I. *Phys. Rev. Lett.* **1989**, *62*, 921.
- (12) Evans, J. W.; Sanders, D. E.; Thiel, P. A.; DePristo, A. E. *Phys. Rev. B* **1990**, *41*, 5410.
- (13) Sanders, D. E.; DePristo, A. E. *Surf. Sci.* **1991**, *254*, 341.
- (14) Gunther, S.; Hitzke, A.; Behm, R. J. *Surf. Rev. Lett.* **1997**, *4*, 1103–1108.
- (15) Hitzke, A.; Huguenschmidt, M. B.; Behm, R. J. *Surf. Sci.* **1997**, *389*, 8–18.
- (16) Yang, Y.-N.; Trafas, B. M.; Luo, Y.-S.; Siefert, R. L.; Weaver, J. H. *Phys. Rev. B* **1991**, *44*, 5720–5725.
- (17) Brune, H.; Wintterlin, J.; Behm, R. J.; Ertl, G. *Phys. Rev. Lett.* **1992**, *68*, 624.
- (18) Venables, J. A. *Philos. Mag.* **1973**, *27*, 697; and references therein.
- (19) Stoyanov, S.; Kashchiev, D. Thin film nucleation and growth theories: A confrontation with experiment. In *Current Topics in Materials Science*; Kaldis, E., Ed.; North-Holland: Amsterdam, 1981; Vol. 7, pp 71, and references therein.
- (20) Evans, J. W.; Bartelt, M. C. Submonolayer nucleation and growth of 2D islands and multilayer mound formation during homoepitaxy. In *Morphological Organization in Epitaxial Growth and Removal*; Zhang, Z., Lagally, M. G., Eds.; World Scientific: Singapore, 1998; Vol. 14; pp 50–72.
- (21) Chang, S.-L.; Thiel, P. A. *CRC Crit. Rev. Surf. Chem.* **1994**, *3*, 239.
- (22) Brune, H. *Surf. Sci. Rep.* **1998**, *31*, 121–229.
- (23) Bartelt, M. C.; Evans, J. W. *Surf. Sci.* **1993**, *298*, 421.
- (24) Bartelt, M. C.; Evans, J. W. *MRS Proc.* **1993**, *312*, 255.
- (25) Feibelman, P. J. *Phys. Rev. B* **1995**, *52*, 12444.
- (26) Yu, B. D.; Scheffler, M. *Phys. Rev. Lett.* **1997**, *77*, 1095.
- (27) Yu, B. D.; Scheffler, M. *Phys. Rev. B* **1997**, *55*, 13916.
- (28) Popescu, M.; Amar, J. G.; Family, F. *Phys. Rev. B* **1998**, *58*, 1613.
- (29) Hughes, B. *Random Walks and Random Environments*; Clarendon Press: Oxford, UK, 1995.
- (30) Evans, J. W.; Flynn-Sanders, D. K.; Thiel, P. A. *Surf. Sci.* **1993**, *298*, 378–383.
- (31) Langelaar, M. H.; Breeman, M.; Boerma, D. O. *Surf. Sci.* **1996**, *352/354*, 597.
- (32) Bartelt, M. C.; Evans, J. W.; Schmid, A. K.; Hwang, R. Q. Island size and environment dependence of adatom capture: Cu/Co Islands on Ru(001). *MRS Proceedings: Mechanisms and Principles of Epitaxial Growth in Metallic Systems*; Wille, L. T., Burmester, C. P., Terakura, K., Comsa, G., Williams, E. D., Eds.; Materials Research Society: Boston, MA, 1998; Vol. 528, pp 253–260.
- (33) Bartelt, M. C.; Schmid, A. K.; Evans, J. W.; Hwang, R. Q. *Phys. Rev. Lett.* **1998**, *81*, 1901.
- (34) Bartelt, M. C.; Stoldt, C. R.; Jenks, C. J.; Thiel, P. A.; Evans, J. W. *Phys. Rev. B* **1999**, *59*, 3125–3134.
- (35) Bartelt, M. C.; Evans, J. W. *Phys. Rev. B* **1996**, *54*, R17359.
- (36) Bartelt, M. C.; Evans, J. W. Exact scaling form for the island size distribution in submonolayer epitaxial growth. *MRS Proceedings: Structure and Evolution of Surfaces*; Cammarata, R. C., Chason, E. H., Einstein, T. L., Williams, E. D., Eds.; Materials Research Society: Boston, MA, 1997; Vol. 440, pp 247–252.
- (37) Bales, G. S.; Chrzan, D. C. *Phys. Rev. B* **1994**, *50*, 6057.
- (38) Bartelt, M. C.; Evans, J. W. *Phys. Rev. B* **1992**, *46*, 12675.
- (39) Gunton, J. D.; Droz, M. *Introduction to the Theory of Metastable and Unstable States*; Springer: Berlin, 1983; Vol. 183.
- (40) Zinke-Allmang, M.; Feldman, L. C.; Grabow, M. H. *Surf. Sci. Rep.* **1992**, *16*, 377.
- (41) Pai, W. W.; Swan, A. K.; Zhang, Z.; Wendelken, J. F. *Phys. Rev. Lett.* **1997**, *79*, 3210.
- (42) Rosenfeld, G.; Esser, M.; Morgenstern, K.; Comsa, G. Ripening mechanisms in ultrathin metal films. *MRS Proceedings: Mechanisms and Principles of Epitaxial Growth in Metallic Systems*; Wille, L. T., Burmester, C. P., Terakura, K., Comsa, G., Williams, E. D., Eds.; Materials Research Society: Boston, MA, 1998; Vol. 528, pp 111–124.
- (43) Stoldt, C. R.; Jenks, C. J.; Thiel, P. A.; Cadilhe, A. M.; Evans, J. W. *J. Chem. Phys.* **1999**, *111*, 5157.
- (44) Rao, M.; Kalos, M. H.; Lebowitz, J. L.; Marro, J. *Phys. Rev. B* **1976**, *13*, 7325.
- (45) Binder, K.; Kalos, M. H. *J. Stat. Phys.* **1980**, *22*, 363–396.



- (46) Voter, A. F. *SPIE—Model. Opt. Thin Films* **1987**, 821, 214.
- (47) Kang, H. C.; Thiel, P. A.; Evans, J. W. *J. Chem. Phys.* **1990**, 93, 9018.
- (48) Soler, J. M. *Phys. Rev. B* **1994**, 50, 5578.
- (49) Khare, S. V.; Bartelt, N. C.; Einstein, T. L. *Phys. Rev. Lett.* **1995**, 75, 2148.
- (50) Sholl, D. S.; Skodje, R. T. *Phys. Rev. Lett.* **1995**, 75, 3158.
- (51) Van Siclen, C. D. *Phys. Rev. Lett.* **1995**, 75, 1574.
- (52) Khare, S. V.; Einstein, T. L. *Phys. Rev. B* **1996**, 54, 11752.
- (53) Bogicevic, A.; Liu, S.; Jacobsen, J.; Lundqvist, B.; Metiu, H. *Phys. Rev. B* **1998**, 57, R9459.
- (54) Morgenstern, K.; Rosenfeld, G.; Comsa, G. *Phys. Rev. Lett.* **1996**, 76, 2113.
- (55) Meakin, P. *Physica A* **1990**, 165, 1.
- (56) Sholl, D. S.; Skodje, R. T. *Physica A* **1996**, 231, 631.
- (57) Mattson, T. R.; Mills, G.; Metiu, H. *J. Chem. Phys.* **1999**, 111, 12151.
- (58) Bardotti, L.; Bartelt, M. C.; Jenks, C. J.; Stoldt, C. R.; Wen, J.-M.; Zhang, C.-M.; Thiel, P. A.; Evans, J. W. *Langmuir* **1998**, 14, 1487–1492.
- (59) Stoldt, C. R.; Cadilhe, A. M.; Bartelt, M. C.; Jenks, C. J.; Thiel, P. A.; Evans, J. W. *Prog. Surf. Sci.* **1998**, 59, 67–77.
- (60) Bartelt, M. C.; Evans, J. W. *Phys. Rev. Lett.* **1995**, 75, 4250.
- (61) Evans, J. W.; Bartelt, M. C. *Langmuir* **1996**, 12, 217.
- (62) Williams, E. D. *Surf. Sci.* **1994**, 299/300, 502.
- (63) Ozcomert, J. S.; Pai, W. W.; Bartelt, N. C.; Reutt-Robey, J. E. *Surf. Sci.* **1993**, 293, 183.
- (64) Stoldt, C. R.; Cadilhe, A. M.; Jenks, C. J.; Wen, J.-M.; Evans, J. W.; Thiel, P. A. *Phys. Rev. Lett.* **1998**, 81, 2950–2953.
- (65) Nelson, R. C.; Einstein, T. L.; Khare, S. V.; Rous, P. J. *Surf. Sci.* **1993**, 295, 462–484.
- (66) Villain, J. *J. Phys. I* **1991**, 1, 19.
- (67) Ehrlich, G.; Hudda, H. *J. Chem. Phys.* **1966**, 44, 1039.
- (68) Schwoebel, R. L.; Shipsey, E. J. *J. Appl. Phys.* **1966**, 37, 3682.
- (69) Barabasi, A.-L.; Stanley, H. G. *Fractal Concepts in Surface Growth*; Cambridge University Press: Cambridge, MA, 1995.
- (70) Yang, H.-N.; Wang, G.-C.; Lu, T.-M. *Diffraction from Rough Surfaces and Dynamic Growth Fronts*; World Scientific: Singapore, 1993.
- (71) Kyuono, K.; Ehrlich, G. *Surf. Sci.* **1997**, 383, L766.
- (72) Elliot, W. C.; Miceli, P. F.; Tse, T.; Stephens, P. W. *Physica A* **1996**, 221, 65.
- (73) Elliot, W. C.; Miceli, P. F.; Tse, T.; Stephens, P. W. *Phys. Rev. B* **1996**, 54, 17938.
- (74) Evans, J. W.; Bartelt, M. C. Submonolayer island formation and subsequent multilayer kinetic roughening during metal(100) homoepitaxy: Fe, Ag, & Cu. In *Surface Diffusion: Atomistic and Collective Processes*; Tringides, M. C., Ed.; Plenum Press: New York, 1997; Vol. 360, pp 197–208.
- (75) Kelchner, C. L.; DePristo, A. E. *J. Vac. Sci. Technol.* **1996**, 14, 1633.
- (76) Kelchner, C. L.; DePristo, A. E. *Surf. Sci.* **1997**, 393, 72.
- (77) Bartelt, M. C.; Evans, J. W. *Surf. Sci.* **1999**, 423, 189–207.
- (78) Nyberg, G. L.; Kief, M. T.; W. F. Egelhoff, J. *Phys. Rev. B* **1993**, 48, 14509.
- (79) Layson, A. R.; Bardotti, L.; Stoldt, C. R.; Thiel, P. A.; Evans, J. W., manuscript in preparation.
- (80) Zhao, Y.-P.; Yang, H.-N.; Wang, G.-C.; Lu, T.-M. *Phys. Rev. B* **1998**, 57, 1922.
- (81) Stroschio, J. A.; Pierce, D. T.; Stiles, M.; Zangwill, A.; Sander, L. M. *Phys. Rev. Lett.* **1995**, 75, 4246.
- (82) Ernst, H. J.; Fabre, F.; Folkerts, R.; Lapujoulade, J. *Phys. Rev. Lett.* **1994**, 72, 112.
- (83) Zuo, J.-K.; Wendelken, J. F. *Phys. Rev. Lett.* **1997**, 78, 2791.
- (84) Icking-Konert, G. S.; Giesen, M.; Ibach, H. *Surf. Sci.* **1998**, 398, 37.
- (85) Tersoff, J.; Denier van der Gon, A. W.; Tromp, R. M. *Phys. Rev. Lett.* **1994**, 72, 266.
- (86) Politi, P.; Villain, J. *Phys. Rev. B* **1996**, 54, 5114.
- (87) Cooper, B. H.; Peale, D. R.; McLean, J. G.; Phillips, R.; Chason, E. *Mater. Res. Soc. Symp. Proc.* **1993**, 280, 37.
- (88) Tsui, F.; Wellman, J.; Xu, J.; Uher, C.; Clarke, R. In *MRS Proceedings: Structure and Evolution of Surfaces*; Cammarata, R. C., Chason, E. H., Einstein, T. L., Williams, E. D., Eds.; Materials Research Society: Boston, MA, 1997; Vol. 440, p 317.
- (89) Villain, J. *Europhys. Lett.* **1986**, 2, 531.
- (90) Zuo, J.-K.; Wendelken, J. F. *Phys. Rev. Lett.* **1993**, 70, 1662.